scientific reports

OPEN

Reducing critical current for spin-transfer-torque magnetization reversal in current-perpendicular-to-plane giant magnetoresistance devices using low damping and spin scattering asymmetry in $Co_2FeGa_{0.5}Ge_{0.5}$ Heusler alloy

Vineet Barwal, Hirofumi Suto✉ & Yuya Sakuraba

Spin-transfer torque (STT) in magnetoresistance devices has enabled key applications such as STT-magnetoresistive random access memory, spin torque oscillators, and energy-assisted magnetic recording. In the device structures, where a free layer (FL) magnetization is manipulated by spin injection from a spin injection layer (SIL), the critical current density required for operation is directly proportional to the damping (α) constant of FL and inversely proportional to the STT efficiency, which depends on the spin polarization (P) of the materials. Here, we investigate the effect of low α and high P of $Co_2FeGa_{0.5}Ge_{0.5}$ (CFGG) Heusler alloy on the operation current required for STT-induced magnetization reversal in current perpendicular-to-plane giant magnetoresistance devices. Devices with CFGG as a FL material achieved a large reduction in the operation current, as compared to those with conventional NiFe-FL owing to the very low α of CFGG, demonstrating the advantage of CFGG as a FL material. As the advantage of high spin polarization CFGG for SIL, we analyzed the effect of bilayer SIL consisting of CoFe and thin CFGG layers, focusing on utilizing the spin scattering asymmetry at the CoFe/CFGG interface. Devices with the CoFe/CFGG-SIL exhibited the lowest critical current, demonstrating enhanced STT efficiency. In addition, the correlation of STT efficiency with magnetoresistance ratio was comprehensively investigated, showing that device-to-device distribution in STT-efficiency was smaller in CoFe/CFGG-SIL. These findings highlight the potential of CFGG Heusler alloy and CoFe/CFGG bilayer structures as key components for the development of efficient and stable STT-based spintronic devices.

Spin-transfer torque (STT) has been widely used to manipulate the magnetization direction of ferromagnets in various spintronic devices such as spin-torque oscillators[1,2], magnetoresistive random-access memory[3,4], and emerging computing devices[5]. In particular, STT realized in current perpendicular-to-plane giant magnetoresistance (CPP-GMR) devices has been extensively studied for assisted writing in hard disk drives (HDDs) to enhance the areal density[6–11]. In this application, STT-based devices are fabricated in the write gap of the write head, and induced magnetization excitation enhances the writability through the flux control (FC) effect[12,13] or the microwave assistance effect[14,15]. Here, we explain the operation principle of FC devices as it is closely related to this study. The simplest FC device has a tri-layer structure consisting of a magnetic free layer (FL), a metallic non-magnetic spacer layer and a magnetic spin injection layer (SIL). SIL is in direct contact and magnetically coupled with the pole materials making the SIL magnetization stable against STT. When a sufficient bias current is applied, STT via spin injection from SIL induces magnetization reversal of FL against the field inside the write gap (gap field). The dipolar field from the reversed FL magnetization can enhance the

Research Center for Magnetic and Spintronic Materials, National Institute for Materials Science (NIMS), Tsukuba 305-0047, Japan. ✉email: SUTO.Hirofumi@nims.go.jp

amplitude and gradient of the write field. The reliable and fast operation of the FC devices has already been demonstrated using actual HDDs[12–14].

One of the primary objectives in these STT-based device applications is to increase the efficiency of magnetization manipulation. In assisted writing, higher efficiency can induce excitation of a larger magnetic volume within the current tolerance of the devices typically of the order of 1×10^8 A/cm^2, to achieve a larger assistance effect[16]. Similarly, in memory and computation applications, higher efficiency reduces the operational current density, thereby lowering power consumption. According to Slonczewski's theory[17], the critical current density of STT-driven magnetization dynamics in CPP-GMR type tri-layer structure is expressed as:

$$J_c = \mu_0 \frac{2|e|}{\hbar \eta} \alpha M_s^{\mathrm{FL}} d H_{\mathrm{eff}} \tag{1}$$

where d, M_s^{FL} and α is the thickness, saturation magnetization and Gilbert damping parameter of FL, respectively. STT efficiency, η is a dimensionless parameter that depends on the spin polarization (P) of the conduction electron in the magnetic layers and the relative angle between magnetization directions of the FL and SIL. H_{eff} is the effective field acting on FL. To reduce the operational current density for STT-induced magnetization manipulation, FL material with low α and SIL materials with high P are beneficial because J_c is directly proportional to α and high P enhances η.

Furthermore, in assisted writing applications, the SIL magnetization counteracts the assistance effect by degrading the recording field. Therefore, reducing the magnetic volume of the SIL is crucial for enhancing the device performance. Thin SIL is also desirable because the total thickness of the device structure need to fit into a small write gap of typically ~ 20 nm[14].

To meet the above requirements, Co-based half-metallic ferromagnet Heusler alloys are promising candidates for use as magnetic layers in STT-based devices due to their theoretically predicted large P ($\sim 100\%$), low α ($\sim 1 \times 10^{-4}$) and high Curie temperature (> 600 K)[3,18–20]. In addition, the Heusler alloys exhibit relatively short spin-diffusion length ($\lambda_{\mathrm{SDL}} \sim 2$–6 nm) which enable them to function effectively as thin layers[21–23]. Among these materials, $Co_2FeGa_{0.5}Ge_{0.5}$ (CFGG) is selected in this study because of the reported low α[24] and theoretically predicted half-metallicity[25,26]. Several studies have reported large magnetoresistance (MR) ratios in CPP-GMR devices incorporating CFGG, demonstrating its potential for enhancing spintronic device performance[23,25,27–34]. The observed large MR ratios are attributed to the high P of CFGG. However, its impact on STT efficiency has not been studied in detail.

In this study, we first performed a detailed structural analysis and evaluated the α of single-layer CFGG Heusler thin films annealed at various temperatures. Subsequently, the CFGG Heusler was incorporated in CPP-GMR devices to investigate the influence of its high P and low α on the MR and STT properties. The significantly lower damping parameter of CFGG compared to conventional NiFe (Py), led to reduction in the critical current required for STT-induced magnetization reversal against an applied magnetic field, demonstrating its potential for efficient STT-based device operation. Furthermore, to leverage the high spin polarization of CFGG for spin injection, we investigated a bilayer SIL composed of CoFe and a thin CFGG layer. The idea of using CoFe/thin CFGG bilayer as SIL is derived from the following two facts: the device structures proposed for assisted writing use SIL attached to CoFe-based magnetic poles[13] and the enhancement in the MR ratio is reported by using the CoFe/CFGG bilayer due to the spin scattering asymmetry at the interface[35]. The use of CoFe/CFGG bilayers as SIL led to a further reduction in operation current with reduced device-to-device distribution. The stable operation and enhanced efficiency achieved with CoFe/CFGG-SIL configurations further underscore their suitability for STT-based devices. These findings highlight the advantages of CFGG as a low-damping FL and CoFe/CFGG as a stable and efficient SIL, making CFGG a promising candidate material for high-performance STT-based devices.

Experimental details
Sample growth and device fabrication
We prepared the following three series of samples by magnetron sputtering on MgO(001) substrates: (A) single-layer CFGG films for structural analysis and α evaluation by ferromagnetic resonance (FMR) measurement, (B) GMR stacks with CFGG and Py as FL, and (C) GMR stacks with CoFe/CFGG bilayers as SIL. The order of the stacking structure is from bottom to top and the numbers in the parentheses represent the nominal thickness in nm, and Py was employed as a reference material. The series-A samples are composed of CFGG(30)/Al(2) films. These films were subjected to in-situ annealing at post-annealing temperature (T_p) of 300, 400, 500 and 600 °C. The Al capping layer was deposited after cooling down the sample to room temperature (RT). Additionally, two control samples with stacking structures Cr(5)/Ag(5)/CFGG(6)/Ru(8) and Cr(5)/Ag(5)/Py(7)/Ru(8) were prepared. In these structures, CFGG and Py thickness were designed to match those of FL configuration in the series-B samples enabling a quantitative estimation of α for the CFGG and Py layers in the CPP-GMR stacks. The CFGG control sample was annealed at $T_p = 500$ °C and cooled down to RT prior to deposition of the Ru layer.

In the series-B and -C samples, Cr(5)/Ag(100) bottom electrode was first deposited and annealed at 300 °C. After cooling the sample down to RT, the GMR stack was subsequently deposited. The series-B samples contain GMR stacks with two different FL configuration: CFGG(15)/Ag(7)/CFGG(6) annealed at $T_p = 500$ °C after the top CFGG layer deposition and CFGG(15)/Ag(7)/Py(7.5) annealed at $T_p = 500$ °C after bottom CFGG layer deposition, which are referred to as CFGG-FL and Py-FL samples, respectively. The bottom 15 nm CFGG layer acted as the SIL, and its higher thickness prevented reversal of the SIL magnetization due to the counter spin injection from FL. Different FL thicknesses were chosen for CFGG-FL and Py-FL to make the FL magnetization volume the same, based on the different M_s of CFGG (1.25 T) and Py (1 T). The GMR stack of series-C samples were composed of CoFe(6)/CFGG(3)/Ag(7)/CFGG(6) and were annealed at $T_p = 350$, 400, 450 and 500 °C after

the deposition of the top CFGG layer. These are referred to as CoFe/CFGG-SIL samples. The choice of the CoFe(6)/CFGG(3) configuration for the SIL is based on two key considerations. First, to effectively utilize the interfacial spin polarization at the CoFe/CFGG interface, the thickness of the CFGG layer was kept comparable to λ_{SDL} (typically ~ 3 nm), allowing spin polarized current to be injected with minimal relaxation[23,28,35,36]. Second, the SIL must maintain a stable magnetization against reverse STT exerted by the 6 nm-thick CFGG FL. To achieve this, a 6 nm-thick CoFe layer is used in the SIL, providing sufficient magnetic volume to ensure magnetic stability.

The annealing time for the series-A and series-B samples was set to 30 min. In contrast, the annealing duration was reduced to 5 min for the series-C sample, to minimize interfacial interdiffusion between CoFe and CFGG layers. A similar short duration annealing was employed in Ref[37], where CPP-GMR structures containing CoFe/$Co_2Fe_{0.4}Mn_{0.6}$Si bilayer electrodes were annealed for 2 min. The annealing temperature in the series-B and the series-C samples was limited to 500 °C as higher temperatures are generally known to cause interdiffusion and degrade the MR output[28,30,31]. The CFGG films were deposited using a composite sputtering target having the composition of $Co_{43.28}Fe_{26}Ga_{15.16}Ge_{15.56}$. The typical composition of the deposited CFGG layer was $Co_{45.20}Fe_{31.90}Ga_{12.69}Ge_{10.21}$, as measured by X-ray fluorescence analysis, calibrated by the standard sample whose composition was analyzed by inductively coupled plasma mass spectrometry. The Co-deficient and Fe-rich off-stoichiometric CFGG composition was chosen to suppress antisites of Co atoms occupying Fe sites, which is detrimental to P, while obtaining single-phase CFGG Heusler films[26,38,39].

Pseudo-spin-valve CPP-GMR devices were fabricated for the series-B and series-C stacks by the following procedure. The samples were patterned into circular and elliptical pillars with lateral dimensions of 200×200 nm^2, 200×100 nm^2, 100×100 nm^2, and 80×80 nm^2 by electron beam lithography and Ar ion milling. Then, the pillars were covered by a thin Ta adhesion layer and a SiO$_2$ passivation layer. After the lift-off of the covering layers, an Au top electrode was fabricated. For each device size, more than 50 devices were prepared on one substrate. The MR measuremenst were conducted on all the devices, and defective devices exhibiting abnormal resistance were excluded from the analysis. The STT measurement was conducted on 80×80 nm^2 devices. Since all devices used for STT measurements have identical lateral dimensions, the switching current I_c is reported instead of current density, allowing for direct comparison without normalization. The circular pillar's cross-sectional area was estimated to be ~ 10.58×10^{-3} μm^2 using scanning electron microscopy. The current amplitude up to 10 mA was typically introduced to the devices, corresponding to the current density of ~ 1×10^8 A/cm^2. Noticeable change in the device properties such as resistance and MR ratio was not observed indicating that the devices have sufficient current durability for practical applications.

Characterization

The structural characterization for the series-A, series-B and series-C sample stacks was done using X-ray diffraction (XRD) with a Cu–K$_\alpha$ radiation source ($\lambda = 1.5406$ Å). The magnetization dynamics properties for the series-A samples were measured by in-plane FMR measurements using broadband FMR set-up in the Physical Property Measurement System (PPMS Dynacool; Quantum Design). The in-plane resonance field ($\mu_0 H_r$) and linewidth ($\mu_0 \Delta H$) were obtained by fitting the FMR spectra to a Lorentzian derivative function containing both symmetric and anti-symmetric components, as detailed in Ref[40]. The damping parameter (α) was then extracted using the following equation.

$$\mu_0 \Delta H = \mu_0 \Delta H_0 + \frac{4\pi\alpha f}{\gamma} \tag{2}$$

where $\mu_0 \Delta H_0$ accounts for line-broadening owing to the extrinsic contributions such as magnetic inhomogeneities, f is the frequency in the GHz range, $\gamma \left(= g\frac{\mu_B}{\hbar}\right)$ is the gyromagnetic ratio with $g \sim 2.1$ as the Lande's factor, μ_B as the Bohr magneton and $\hbar$ as the reduced Planck's constant.

Resistance versus magnetic field (R-H) measurements were conducted on the CPP-GMR devices fabricated from the series-B and series-C samples through the four-probe measurement method. The measurement was done in an auto-prober system by applying in-plane magnetic field along the long axis of the elliptical pillars. MR ratio was defined as $(R_P - R_{AP})/R_P \times 100\%$, where R_P and R_{AP} are the resistance in the parallel (P) and anti-parallel (AP) configuration of the FL and SIL. The STT induced magnetization reversal against the magnetic field measurements were conducted on the CPP-GMR devices from the series-B and series-C samples having circular pillars with a designed diameter of 80 nm. The details of the measurement method can be found in the Ref[41,42].

Results and discussion
Series-A single-layer CFGG films
Structural characterization
XRD measurements were performed to study the effect of annealing temperature on the structural properties of the series-A single layer CFGG films. Figure 1a shows the out-of-plane XRD profiles at $\chi = 0°$ for the series-A samples. The XRD profiles show only the diffraction peaks corresponding to the (001) plane, indicating (001)-oriented growth. The 002 Heusler peak confirms $B2$ ordering, reflecting the atomic order between Co and (Fe, Ga, Ge) sites in all the samples. The increasing intensity of 002 peak with higher T_p, suggests improved $B2$ ordering. Figure 1b shows the corresponding XRD profiles along the [111] direction at $\chi = 54.7°$. A faint 111 superlattice diffraction peak is observed for $T_p = 500$ °C sample and becoming more prominent at $T_p = 600$ °C, indicating the enhancement of $L2_1$ ordering, which reflects atomic ordering between Fe, and (Ga, Ge) sites. The lattice mismatch between CFGG and MgO is estimated to be < 3.7% from the lattice parameter, $a = 0.574$ nm for the CFGG and $\sqrt{2}\, a = 0.595$ nm for MgO. The lattice parameter matches well with the reported bulk value,
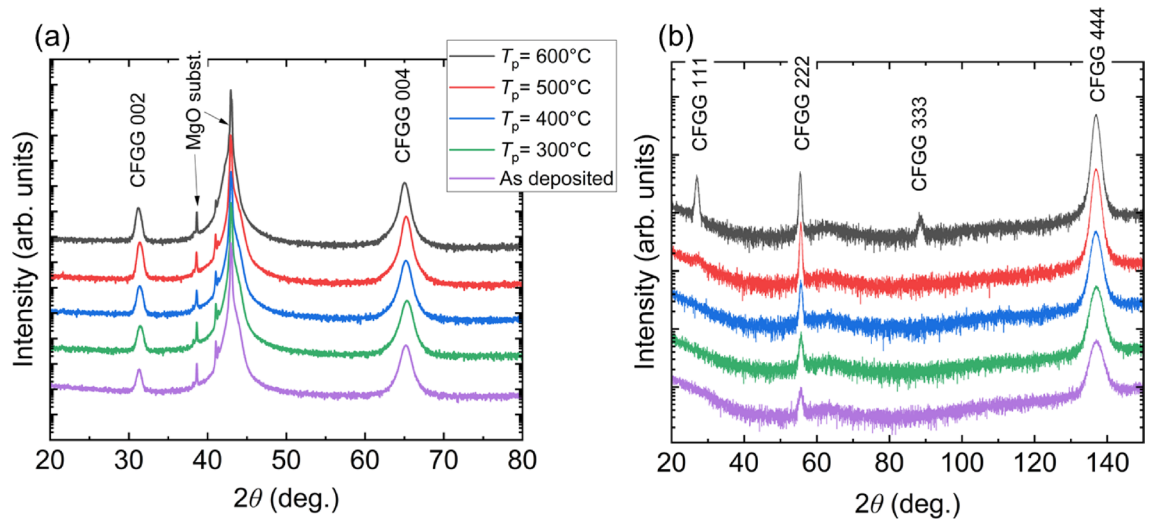
Fig. 1. Out-of-plane XRD profiles at (**a**) $\chi = 0°$ and (b)$\chi = 54.7°$ for the series-A CFGG thin films with different annealing temperature of RT, 300, 400, 500, and 600 °C. The legends are common for (**a**) and (**b**) and data are offset for clarity.
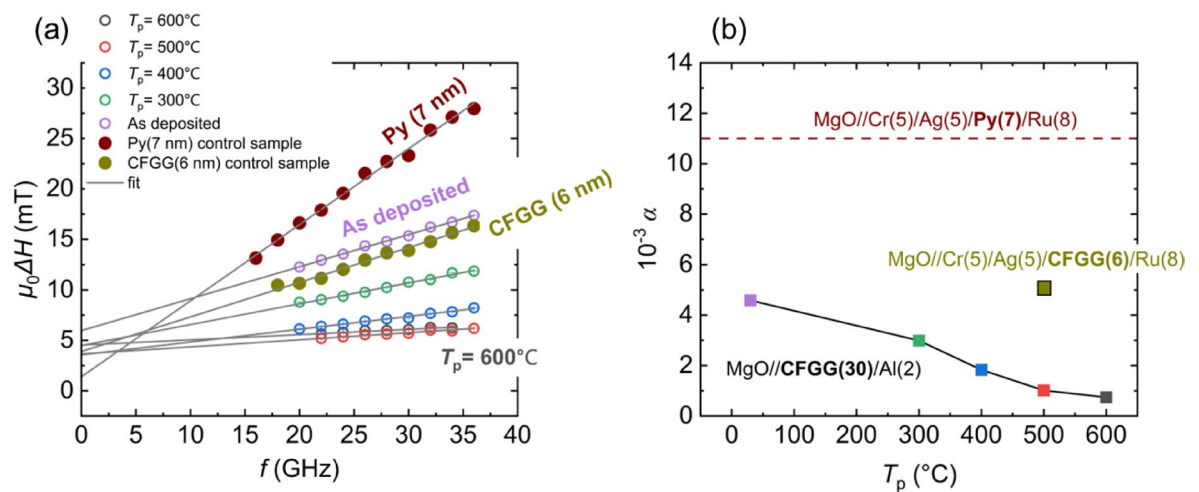

Fig. 2. (**a**) FMR linewidth (ΔH) vs. frequency (f) data for the series-A samples, fitted using Eq. (2). Symbols represent the experimental data and lines are the fit. (**b**) Change in damping parameter (α) with T_p in the series-A samples, represented by solid square symbols. The α for the 500 °C annealed CFGG control sample is shown by dark yellow square block and the α for the Py control sample is represented by a dotted wine color line.

exhibiting values within the range of 0.572–0.573 nm with different T_p. The measured XRD profiles for the control samples are shown in the Supplementary Fig. S1.

Damping parameter

In-plane FMR measurements were performed for the series-A samples to elucidate the effect of T_p on the α of the CFGG films. Supplementary Fig. S2a shows the FMR spectra recorded for the 500 °C annealed CFGG control sample. Figure 2a shows the f dependence of $\mu_0 \Delta H$ data fitted using Eq. (2) to extract the α. The offset, $\mu_0 \Delta H_0$, representing inhomogeneities of the samples is higher in CFGG than in Py, which might be due to the inhomogeneous quality of the CFGG films. Figure 2b shows the variation of α for the series-A samples. For the 30 nm CFGG films, α decreased monotonically from 0.00459 in the as-deposited sample to 0.00074 in the $T_p = 600$ °C sample. The reduction in α with increasing T_p can be attributed to enhanced atomic ordering[25,39], as indicated by the XRD measurements.

To evaluate the effect of α of the FL on the critical current required for magnetization reversal against an applied magnetic field, α was measured for the control samples having structure similar to the FL in the series-B CPP-GMR stacks. The CFGG control sample with 6 nm thickness exhibited a higher α compared to the 30 nm thick CFGG film annealed at the same T_p. Generally, α increases with decreasing thickness due to enhanced

interfacial effects[43] such as spin-pumping[44,45]. However, the α value for CFGG control sample is approximately 60% lower than that of Py control sample. This lower damping in CFGG is critical for reducing the critical current of the device operation, as discussed later.

Series-B and -C CPP-GMR stacks

Structural characterization

Figure 3a shows the CPP-GMR stack structure for the series-B and series-C samples. Figure 3b shows the out-of-plane XRD pattern measured at $\chi = 0°$ for the series-B samples. The observed diffraction peaks corresponding to the (001) plane of Cr, Ag, and CFGG, indicates the (001)-oriented growth. The presence of a superlattice 002 peak from the CFGG layer confirms B2 ordering. The diffraction peak corresponding to the Py (220) plane was observed in the Py-FL sample. Figure 3c shows the XRD pattern measured at $\chi = 54.7°$, where a 111 superlattice diffraction peak is observed, indicating the presence of $L2_1$ ordering in the CFGG layer. Figure 3d, e shows the XRD profiles at $\chi = 0°$ and $\chi = 54.7°$ for the series-C samples, respectively. Similar to the series-B samples, (001)-oriented growth and B2 ordering of the CFGG layer was observed. The intensity of the CFGG 002 peak increases with the T_p, indicating improved B2 ordering. Note that the CoFe 002 peak appears close to the Cr 002 and CFGG 004 peaks, making it difficult to distinguish. The CFGG 002 intensity is lower than that in the series-B samples due to the reduced CFGG thickness. The CFGG 111 superlattice peak is not observed for $T_p = 350 – 450°C$ and appears weakly at $T_p = 500°C$. Pendellösung fringes are observed in the series-C samples as well as series-B CFGG-FL sample, typically seen in superlattice structures, indicating good interface quality and film uniformity.

Magnetotransport measurement (I): MR measurement

R-H measurements were performed on the CPP-GMR devices from the series-B and series-C samples to evaluate their MR properties. Representative *R-H* curves for the CPP-GMR devices from both the series are shown in the Supplementary Fig. S3, where the AP configuration of FL and SIL is stabilized by the dipolar interaction at zero magnetic field.

Figure 4 shows the MR ratio distribution for the devices. In comparison between the Py-FL and CFGG samples, the CFGG-FL sample exhibited significantly higher average MR ratio (MR$_{avg}$), reaching 24.37%, which indicates that using CFGG in both FL and SIL is more advantageous for achieving large MR due to its high *P* and the good electronic band matching at the interface with the Ag spacer[28,29]. Additionally, the distribution of MR ratios broadened, which can be attributed to device-to-device inhomogeneities in quality of the CFGG layers. Namely, devices with high B2 as well as $L2_1$ atomic order in the CFGG layers are expected to have high *P* in these layers, leading to large MR ratio[46,47]. As the CFGG-FL sample has two CFGG layers, the effect of the CFGG layer quality is larger than in the Py-FL sample. These results are consistent with the FMR measurement, where CFGG films exhibited inhomogeneous broadening.
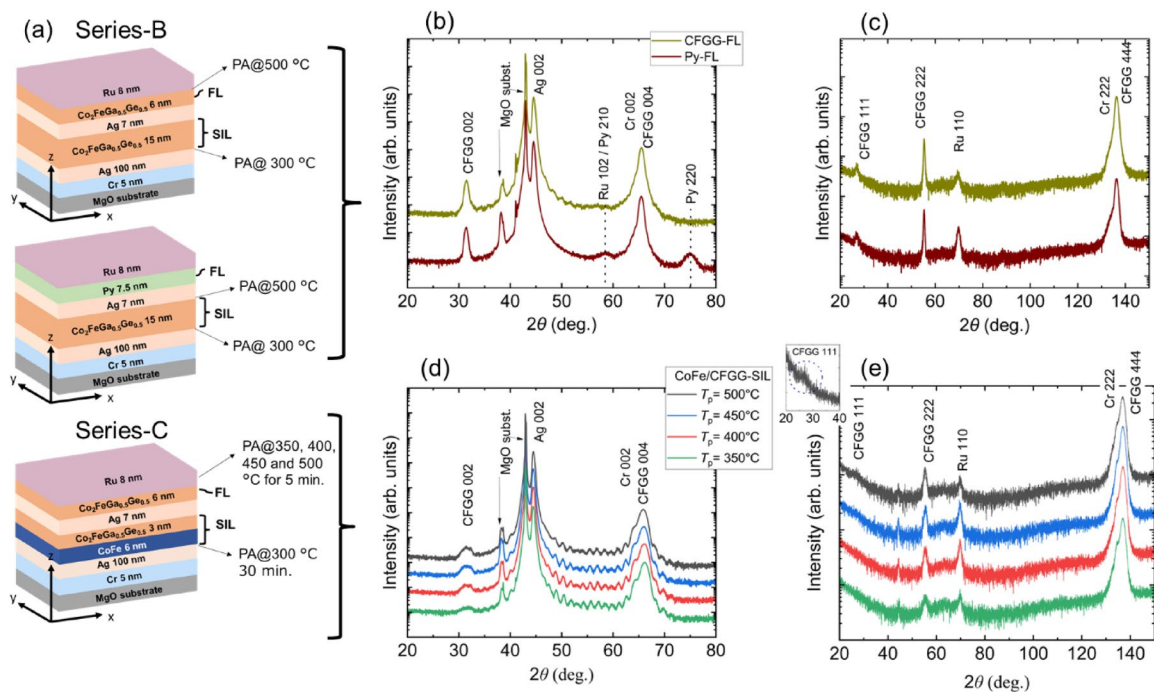

Fig. 3. (**a**) CPP-GMR stack structures for the series-B and series-C samples. XRD profiles at (**b**) $\chi = 0°$ and (**c**) $\chi = 54.7°$ for the series-B samples. XRD profiles at (**d**) $\chi = 0°$ and (**e**) $\chi = 54.7°$ for the series-C samples. Inset in (**e**) shows the zoomed image of the XRD scan for the CoFe/CFGG-SIL ($T_p = 500$ °C) sample around the CFGG 111 peak. The legends are common for (**b**) and (**c**), and for (**d**) and (**e**), with data offset for clarity.
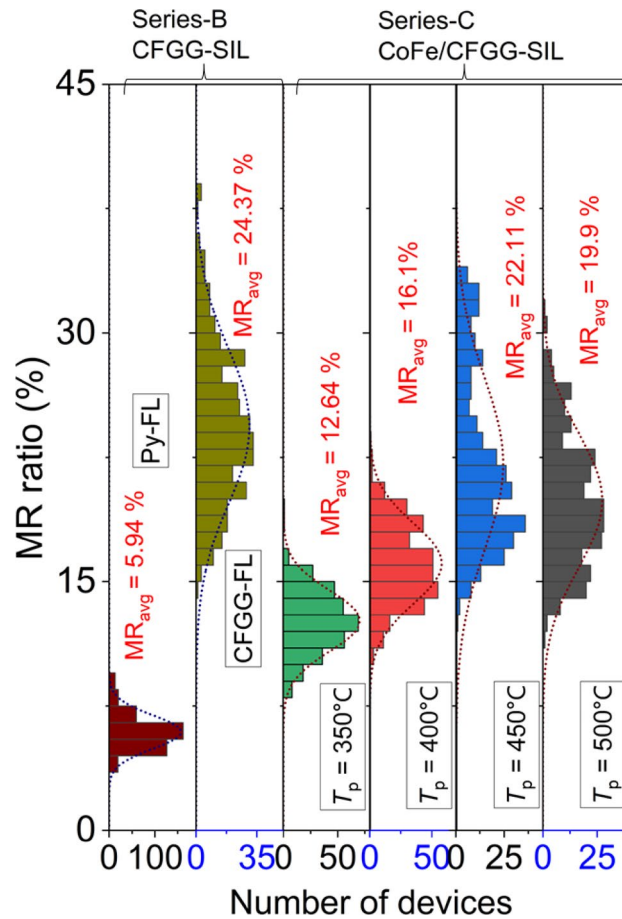
Fig. 4. Distribution of MR ratio in the CPP-GMR devices for the series-B and series-C samples represented by coloured histograms. The abscissa represents the number of devices in each MR ratio interval, as shown on the ordinate axis. Inset in each histogram displays the average MR ratio (MR_{avg}).

The series-C samples exhibit higher MR_{avg} than the Py-FL sample because of the use of CFGG in both FL and SIL. The MR_{avg} increased with T_p due to the improved atomic ordering of CFGG, reaching a peak of 21.96% at $T_p = 450$ °C, which is followed by a slight decline at $T_p = 500$ °C. The distribution of MR increased with T_p, presumably reflecting the CFGG quality, as discussed above. These results indicate that 450 °C is the optimal annealing temperature for the CoFe/CFGG-SIL devices. The decrease at $T_p = 500$ °C might be related to the interdiffusion at the CoFe/CFGG interface.

Magnetotransport measurement (II): STT measurement
We investigated the impact of low damping and high spin polarization of CFGG on STT-efficiency by measuring STT-induced FL magnetization reversal against the magnetic field. Figure 5a, b show the exemplary resistance versus bias current (R-I_b) curves for the series-B Py-FL and CFGG-FL samples, respectively, measured at several perpendicular magnetic fields ($\mu_0 H_z$). The $\mu_0 H_z$ values were sufficiently high to align the magnetization of both the FL and SIL parallel to the $\mu_0 H_z$ direction at zero I_b. The parabolic increase in resistance observed for both positive and negative biases in the R-I_b curves is attributed to Joule heating. At negative bias, where electron flows from the FL to the SIL, an additional step in the device resistance is observed when a sufficiently large negative I_b is applied, and this step corresponds to the magnetization reversal of FL detected through the MR effect. The sign of I_b required for the reversal agrees with the expected behavior of STT-induced FL reversal. Additionally, the magnitude of the bias current necessary to induce the magnetization reversal increases with $\mu_0 H_z$ because higher H_z requires stronger STT for the FL magnetization reversal.

Notably, the magnetization reversal behavior differs significantly between the Py-FL and CFGG-FL samples. The Py-FL sample exhibits a gradual change in resistance with I_b, indicating gradual magnetization reversal from P to AP configuration. In contrast, the CFGG-FL sample exhibits a steep resistance change, suggesting abrupt reversal of the FL magnetization. The different behavior of FL magnetization reversal is explained as follows, based on discussion in Ref.[48]. In the P configuration, STT acting on the FL magnetization is stronger for the Py-FL sample because of the spin accumulation arising from the mismatch in P between Py FL and CFGG SIL, whereas the CFGG-FL sample have small spin accumulation due to matched P in the FL and SIL, resulting in weak STT. In the AP configuration, however, STT becomes stronger for the CFGG-Py sample as high P in both FL and SIL leads to large P mismatch when their magnetization directions are the opposite, enhancing spin
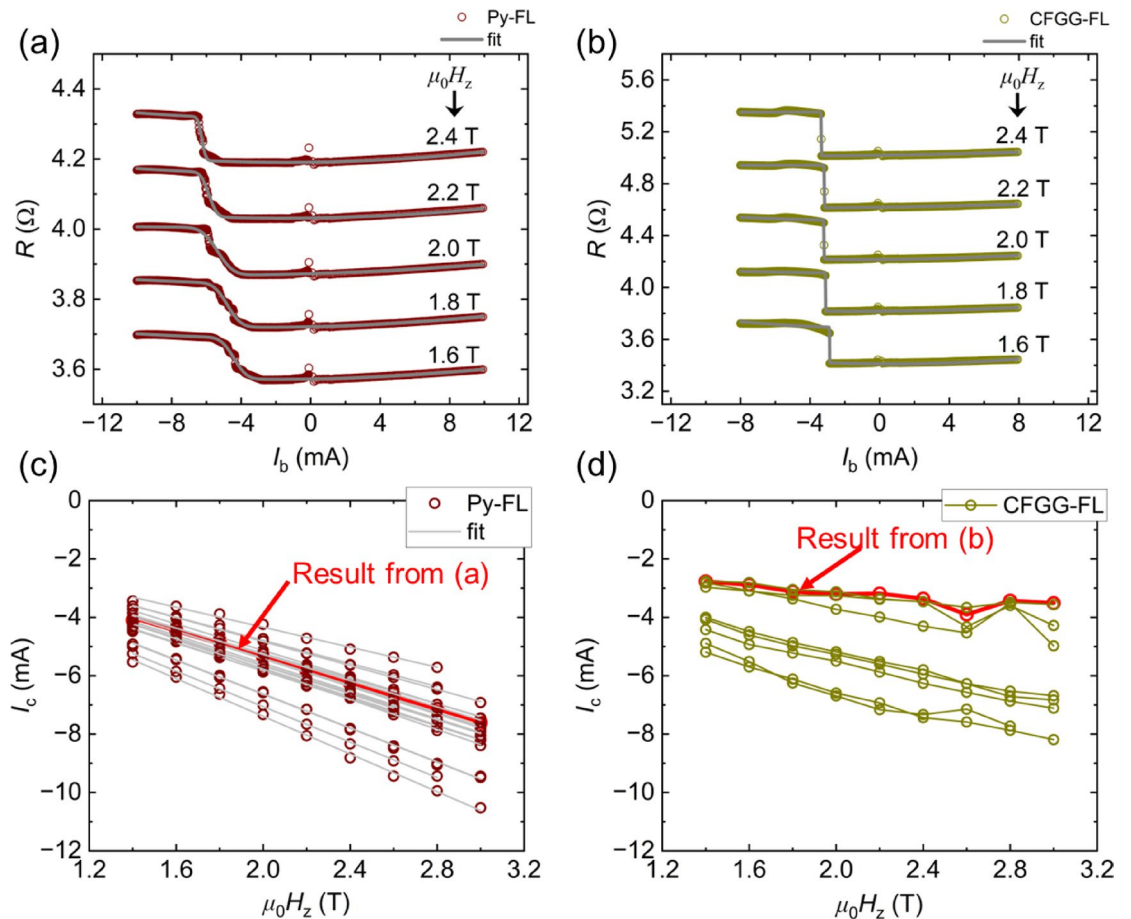
Fig. 5. Exemplary R-I_b curves at several constant $\mu_0 H_z$ values for the CPP-GMR device from the series-B (**a**) Py-FL and (**b**) CFGG-FL samples. The curves are offset for clarity. Variation of critical current (I_c) with $\mu_0 H_z$ for several devices from the series-B (**c**) Py-FL and (**d**) CFGG-FL samples. Note: All STT measurements were conducted on devices with a standardized lateral dimension of 80×80 nm^2. As the element sizes are identical, I_c are directly comparable and are used in place of current density.

accumulation. These considerations mean that the dependence of STT on the magnetization configuration is larger for the CFGG-FL sample. Consequently, in the Py-FL sample, as the magnetization reversal progresses, increased damping torque requires more STT to maintain balance between STT and damping torque, leading to gradual transition with I_b. In contrast, in the CFGG-FL sample, once the magnetization reversal starts, increased damping torque is outpaced by increased STT, resulting in steep transition.

The R-I_b curves were fitted phenomenologically using the following equation:

$$R = f\left(I_b\right) + \frac{\Delta R}{2}\left(1 + \mathrm{erfc}\left(\frac{I_b - I_c}{I_{\mathrm{width}}}\right)\right), \tag{3}$$

where f is a second-order polynomial function representing the change in resistance (R) due to temperature, ΔR represents the change in R due to the magnetization reversal, erfc is the error function, I_c is the critical current corresponding to the I_b value at the center of the R change, and I_{width} is the I_b width of the R change covering approximately 85% of the R change.

Figure 5c, d show the variation of I_c with $\mu_0 H_z$ for several devices from the series-B Py-FL and CFGG-FL samples, respectively. The I_c values exhibit a linear change with $\mu_0 H_z$ as predicted by the theory. Although the I_c values exhibited device-to-device distribution similar to the MR property, the CFGG-FL sample overall shows lower I_c than the Py-FL sample, demonstrating that lower α of CFGG can reduce the current required for the magnetization reversal.

The I_c versus $\mu_0 H_z$ data for the Py-FL sample were linearly fitted using Eq. (1) to determine the STT efficiency, η. For fitting, the following parameters were used for Py: thickness (d) ~ 7 nm, M_s^{FL} ~ 0.9 T and α ~ 0.011. The resulting η for CFGG was found to be around ~ 0.6, which is higher than the typical value of ~ 0.4 reported for the conventional CoFe system[42], indicating a high STT efficiency due to high P in the CFGG layer. A comparable value of η has been previously reported for the $Co_2Mn_{1-x}Fe_xGe$ ($0 \leq x \leq 0.8$) Heusler alloy in CPP-GMR devices[49]. The CFGG-FL sample data were not analyzed by this model as it considers the case where magnetization reversal evolves gradually with the bias current and is not applicable to abrupt magnetization reversal observed in the

CFGG-FL sample. The R-I_b curves for the CFGG-FL sample were fitted solely to extract the I_c values for the comparison with those of the Py-FL sample.

Figure 6a shows the exemplary R-I_b curves measured at various constant $\mu_0 H_z$ ranging from 1.4 T to 3 T in a CPP-GMR device from the CoFe/CFGG-SIL (annealed at $T_p = 500$ °C) series-C sample. Resistance steps appear in the negative I_b, indicating STT-induced magnetization reversal in the device. The R-I_b curves were fitted using Eq. (3) to extract I_c. Figure 6b shows the variation of I_c as a function of $\mu_0 H_z$ for a representative device. At fields greater than 2.2 T, the magnitude of I_c increases with $\mu_0 H_z$ similar to the results from the series-B samples. However, at lower $\mu_0 H_z$ values less than 2.2T, the I_c magnitude decreases with $\mu_0 H_z$. Furthermore, the resistance steps in Fig. 6a are smaller in this low field ($\mu_0 H_z < 2.2$T) range compared to those at higher field range ($\mu_0 H_z > 2.2$T), suggesting that a complete AP configuration state was not achieved, even under high bias current. This difference between the lower and higher $\mu_0 H_z$ range is explained as follows. At lower H_z, the magnetization of the CoFe/CFGG SIL may not be fully aligned with the applied perpendicular field because of the larger demagnetization field associated with the high M_s of CoFe (2.4 T). The resulting tilt in the SIL magnetization prevents complete AP configuration and reduces STT efficiency, resulting in different reversal behavior. Notably, the M_s value closely aligns with the field value, at which the magnetization reversal behavior changed, supporting the above discussion. Additionally, due to insufficient H_z, the SIL magnetization might be unstable under counter STT from the spin injection by the FL, which also prevents complete AP configuration. By applying a sufficiently high H_z, the SIL magnetization aligns perpendicularly and stabilizes, enabling only the FL magnetization to reverse as designed.

Figure 7a–d show the variation of I_c values with $\mu_0 H_z$ for the CPP-GMR devices from the series-C samples, annealed at different temperatures: 350 °C, 400 °C, 450 °C and 500 °C, respectively. Across all samples, the I_c magnitude exhibits a consistent trend: initially decreasing with increasing $\mu_0 H_z$ up to approximately 2.2 T, followed by a subsequent linear increase as $\mu_0 H_z$ is further increased. A distribution in I_c values was observed, which correlates with the MR ratio of the devices, as discussed below.

To better understand the distribution of I_c and its correlation with the MR ratio, the I_c values at $\mu_0 H_z = 2.4$ T were plotted against the MR ratios, as shown in Fig. 8a. We first focus on the results from the series-B samples. As previously discussed, the CFGG-FL sample exhibit lower I_c magnitude than the Py-FL sample due to low α of CFGG as compared to Py. When we compare the best devices from the CFGG-FL and Py-FL samples, the I_c magnitude decreased from -5.1 mA to -3.4 mA, representing a $\sim 33\%$ reduction. Based on the SEM-estimated pillar area, the corresponding current density dropped from 4.8×10^7 A/cm² to 3.2×10^7 A/cm². This reduction in the I_c magnitude is smaller than the 60% decrease in α from Py to CFGG, despite the expectation that I_c is proportional to α. One main reason for this discrepancy might be the different magnetization reversal behavior of the FL between the Py-FL sample and CFGG-FL samples, which exhibit gradual and abrupt magnetization reversal, respectively. In the Py-FL sample, the FL magnetization is in the middle of the reversal process at I_c. In contrast, in the CFGG-FL sample, magnetization reversal is initially hindered by a weak STT in the P configuration, and once the threshold to initiate magnetization reversal is overcome at I_c, FL undergoes a complete and abrupt transition. This difference complicates a direct comparison of I_c between the two samples and may lead to an underestimation of the reduction in I_c. Additionally, the structure of the control samples used for FMR measurement is not exactly the same as that of the GMR stacks although the thickness and capping are similarly designed. This is because FMR samples require only a single magnetic layer for precise measurement. The structural difference suggests that spin pumping effects originating from the bottom side of FL could enhance α, potentially leading to the discrepancy between α and I_c reduction.

It is important to note that the penetration depth of the transverse spin current, over which the transfer of spin angular momentum occurs, is typically less than 2 nm in ferromagnets[50]. The thicknesses of the Py-FL and
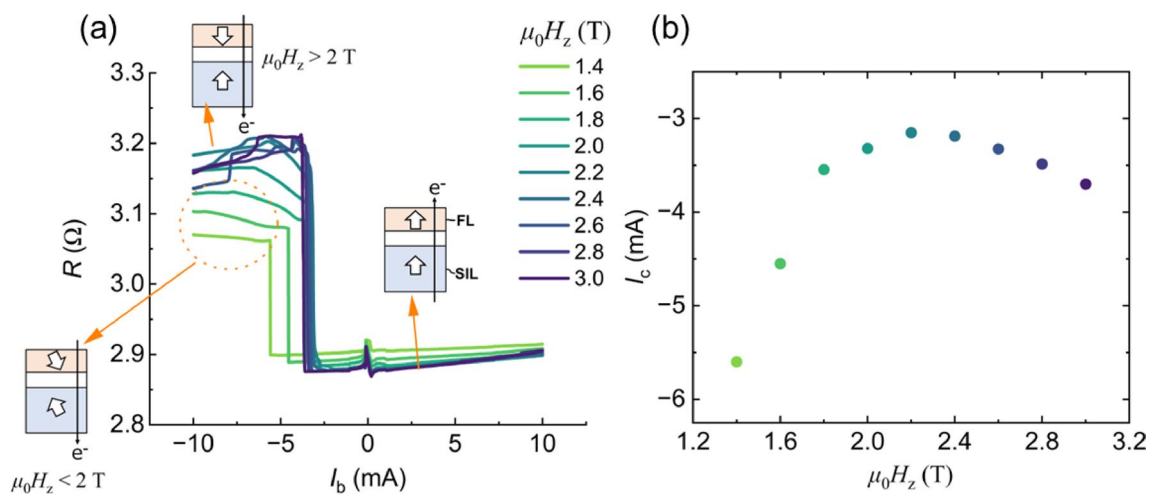

Fig. 6. (**a**) R-I_b curves at several constant $\mu_0 H_z$ values and (**b**) variation of critical current (I_c) with $\mu_0 H_z$ for the MR device from the CoFe/CFGG ($T_p = 500$ °C) series-C sample. Schematics in the inset of (**a**) shows the P, AP and incomplete-AP state configuration for the FL and SIL layer magnetizations.
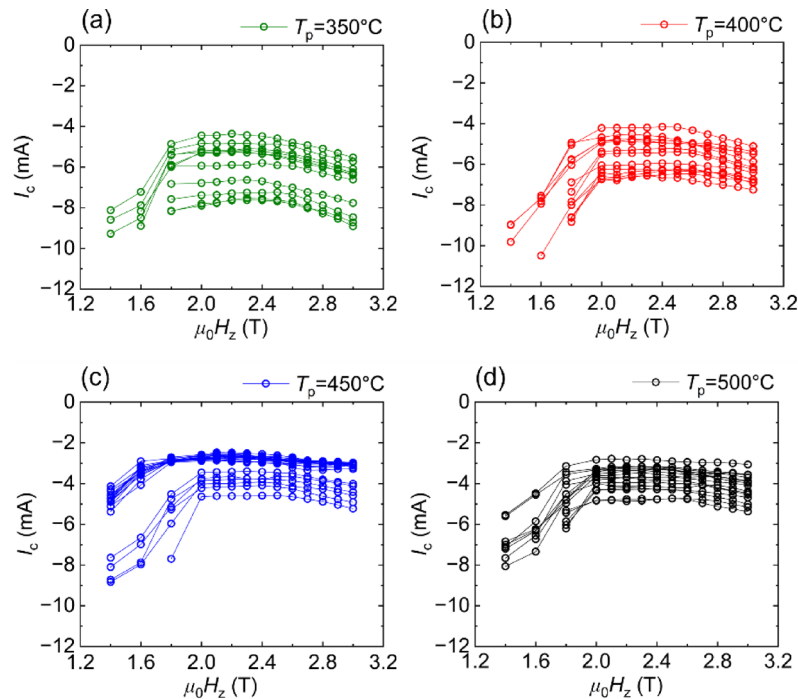
Fig. 7. Variation of critical current (I_c) with $\mu_0 H_z$ for several MR devices from the series-C samples at different annealing temperatures: (**a**) $T_p = 350$ °C, (**b**) $T_p = 400$ °C, (**c**) $T_p = 450$ °C and (**d**) $T_p = 500$ °C.

CFGG-FL are sufficiently higher than this typical transverse spin diffusion length, meaning that the angular momentum of the injected transverse spins is fully transferred to the magnetization. Therefore, the thickness difference in Py-FL and CFGG-FL should not influence the analysis on STT.

Both CFGG-FL and Py-FL samples show an overall positive correlation between the I_c and MR ratio in the device-to-device distributions. This trend is attributed to the fact that devices with high-quality CFGG-SIL layers are expected to show large MR and high η simultaneously because of high P, leading to reduction in the I_c magnitude. Additionally, in the CFGG-FL samples, devices with high-quality CFGG-FL are expected to have low α in the FL as low α is related to high P of CFGG, influencing the correlation between the I_c and MR.

For the series-C CoFe/CFGG-SIL samples, the I_c magnitude decreased with an increase in T_p from 350°C to 450 °C, followed by a slight increase at 500°C. This trend is consistent with that of the MR ratio and is attributed to the increased P and reduced α of the CFGG layers due to the enhanced atomic ordering. The sample annealed at $T_p = 450$ °C exhibited the lowest I_c of approximately -2.5 mA ($J_c \sim 2.4 \times 10^7$ A/cm^2) at $\mu_0 H_z = 2.4$ T. As with the series-B samples, the device-to-device distributions in the I_c and MR ratio in the series-C samples showed a general positive correlation, for the same reason discussed above.

Figure 8b shows the box plots for the I_c distributions in the series-B and series-C samples. Each box represents the interquartile range of 25–75% of the I_c values for the corresponding sample, with the median indicated as a horizontal line within the box. The white diamond in each box denotes the mean I_c. Whiskers extend to 1.5 times the interquartile range, representing the I_c range within which most data points fall. Outliers are represented as dots beyond the whiskers. Remarkably, the CoFe/CFGG-SIL ($T_p = 450$ °C) sample exhibit a very narrow I_c distribution, in comparison to the other CoFe/CFGG-SIL samples with different T_p and the CFGG-FL sample. This suppression in the I_c distribution is interesting considering that the MR ratio distribution is similarly broad in both CoFe/CFGG-SIL ($T_p = 450$ °C) and CFGG-FL sample. These results demonstrate that CoFe/CFGG-SIL is effective in realizing stable STT, leading to reliable operation in the STT-based devices. One possible reason for this stable STT is that CoFe/CFGG SIL is more robust to counter spin injection than single-layer CFGG SIL because CoFe has higher α than CFGG. The magnetization instability of single-layer CFGG SIL affects spin injection, leading to the distribution in I_c. This speculation is supported by the comparison between the Py-FL and CFGG-FL samples, where distribution in the I_c versus MR trend is larger and non-monotonic in the CFGG-FL sample because the counter spin injection is stronger in the CFGG-FL sample due to the high P of FL. Another possible reason is that the contributions of the CoFe/CFGG bilayer structure to the effective SIL spin polarization are stable against variations in the atomic ordering of CFGG.

Figure 8c shows the R_{min} values of the devices plotted against their corresponding MR ratio whose I_c data are presented in Fig. 8a. Confirming R_{min} is necessary to get insight into the device size distribution, as I_c is sensitive to cross-sectional area. This analysis was performed across multiple devices from different samples, with nominal 80×80 nm^2 lateral dimensions. Note that the MR ratio is less sensitive to the device size as the MR ratio is normalized by R_{min}. The R_{min} values are stable within the multiple devices from the same samples, indicating that the I_c distribution primarily reflects the materials parameters and not of the device size. For the series-C samples annealed at $T_p = 350$ °C and 400 °C, R_{min} was slightly higher, although the procedure for
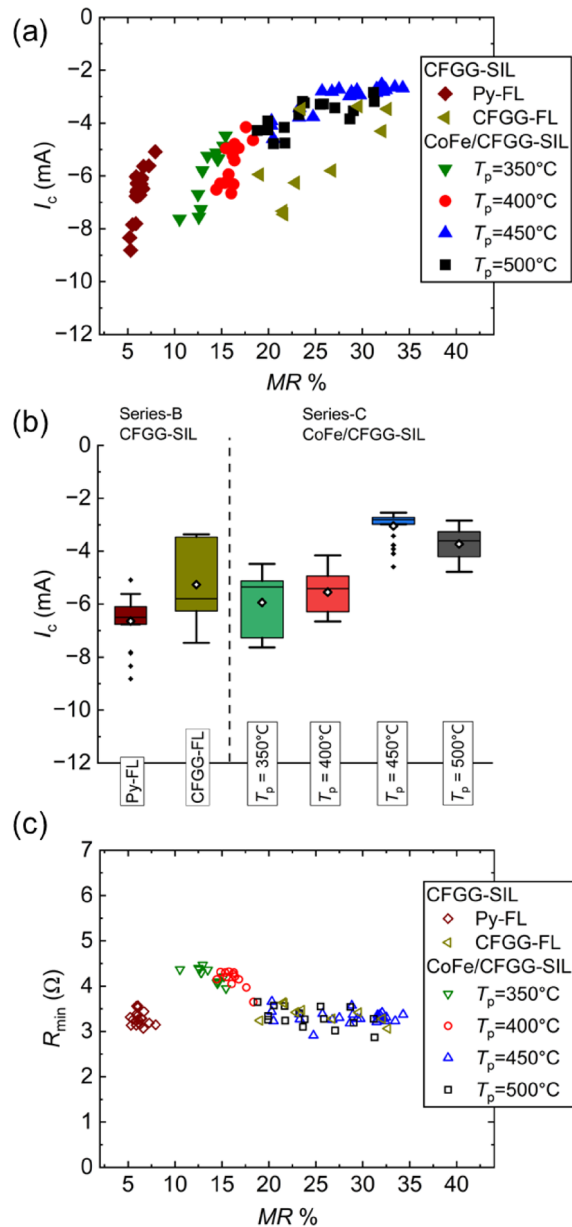
Fig. 8. (**a**) Critical current (I_c) at $\mu_0 H_z = 2.4$ T plotted against the MR ratios for the measured devices from the series-B and series-C samples. (**b**) Box plots displaying the distribution of I_c for the same data set shown in panel (**a**), highlighting statistical variation across different samples, (**c**) resistance in the parallel state (R_{min}) plotted against the MR ratio for the devices corresponding to the data in panel (**a**). All STT data presented correspond to devices patterned with standardized 80×80 nm² lateral dimensions.

the device fabrication is the same among the samples. This increase in R_{min} is due to the increased resistivity of the CFGG layer at lower T_p likely originating from the reduced atomic ordering in the CFGG layers, as shown in the Supplementary Fig. S4. Overall, the influence of device size distribution on the presented results can be considered minimal.

Conclusion

We investigated the CFGG Heusler alloy in CPP-GMR devices to explore its potential in reducing operational current of STT-induced magnetization reversal, leveraging its high P and low α. In comparison between devices using CFGG and Py as the FL, CFGG-based devices demonstrated a 33% reduction in operational current, attributed to its lower α. Furthermore, incorporating a bilayer SIL composed of CoFe and thin CFGG layers led to an additional reduction in operational current, due to spin scattering asymmetry at the CoFe/CFGG interface. The correlation between STT efficiency and MR ratio was thoroughly studied, revealing reduced device-to-device variation in operational current in devices incorporating CoFe/CFGG-SIL structures. These findings

demonstrate the advantages of CFGG as a low-damping FL material and CoFe/CFGG as a stable and efficient SIL, establishing CFGG as a promising candidate material for high-performance STT-based spintronic devices.

Data availability

References

1. Dumas, R. K. et al. Recent advances in nanocontact spin-torque oscillators. *IEEE Trans. Magn.* **50**, 4100107 (2014).
2. Chen, T. et al. Spin-torque and spin-hall nano-oscillators. *Proc. IEEE* **104**, 1919–1945 (2016).
3. Hirohata, A. et al. Review on spintronics: Principles and device applications. *J. Magn. Magn. Mater.* **509**, 166711 (2020).
4. Bhatti, S. et al. Spintronics based random access memory: a review. *Mater. Today* **20**, 530–548 (2017).
5. Locatelli, N., Cros, V. & Grollier, J. Spin-torque building blocks. *Nat. Mater.* **13**, 11–20 (2014).
6. Zhu, J.-G., Zhu, X. & Tang, Y. Microwave assisted magnetic recording. *IEEE Trans. Magn.* **44**, 125–131 (2008).
7. Zhu, J. & Wang, Y. Microwave assisted magnetic recording utilizing perpendicular spin torque oscillator with switchable perpendicular electrodes. *IEEE Trans. Magn.* **46**, 751–757 (2010).
8. Okamoto, S., Kikuchi, N., Furuta, M., Kitakami, O. & Shimatsu, T. Microwave assisted magnetic recording technologies and related physics. *J. Phys. D Appl. Phys.* **48**, 353001. https://doi.org/10.1088/0022-3727/48/35/353001 (2015).
9. Bosu, S. et al. High frequency out-of-plane oscillation with large cone angle in mag-flip spin torque oscillators for microwave assisted magnetic recording. *Appl. Phys. Lett.* **110**, 142403 (2017).
10. Zhou, W. et al. Inducing out-of-plane precession of magnetization for microwave-assisted magnetic recording with an oscillating polarizer in a spin-torque oscillator. *Appl. Phys. Lett.* **114**, 172403 (2019).
11. Sepehri-Amin, H. et al. Design of spin-injection-layer in all-in-plane spin-torque-oscillator for microwave assisted magnetic recording. *J. Magn. Magn. Mater.* **476**, 361–370 (2019).
12. Narita, N. et al. Design and numerical study of flux control effect dominant MAMR head: FC writer. *IEEE Trans. Magn.* **57**, 3300205 (2021).
13. Suto, H. et al. Magnetization dynamics of a flux control device fabricated in the write gap of a hard-disk-drive write head for high-density recording. *J. Appl. Phys.* **129**, 103901 (2021).
14. Takagishi, M. et al. Design concept of MAS effect dominant MAMR head and numerical study. *IEEE Trans. Magn.* **57**, 3300106 (2021).
15. Suto, H. et al. Subnanosecond microwave-assisted magnetization switching in a circularly polarized microwave magnetic field. *Appl. Phys. Lett.* **110**, 262403 (2017).
16. Takagishi, M. et al. Journal of magnetism and magnetic materials microwave assisted magnetic recording : Physics and application to hard disk drives. *J. Magn. Magn. Mater.* **563**, 169859 (2022).
17. Slonczewski, J. C. Current-driven excitation of magnetic multilayers. *J. Magn. Magn. Mater.* **159**, L1–L7 (1996).
18. Kubota, T., Wen, Z. & Takanashi, K. Current-perpendicular-to-plane giant magnetoresistance effects using Heusler alloys. *J. Magn. Magn. Mater.* **492**, 165667 (2019).
19. Elphick, K. et al. Heusler alloys for spintronic devices: Review on recent development and future perspectives. *Sci. Technol. Adv. Mater.* **22**, 235–271 (2021).
20. Hirohata, A. & Lloyd, D. C. Heusler alloys for metal spintronics. *MRS Bull.* **47**, 593–599 (2022).
21. Nakatani, T. M. et al. Bulk and interfacial scatterings in current-perpendicular-to-plane giant magnetoresistance with Co2Fe(Al0.5Si0.5) Heusler alloy layers and Ag spacer. *Appl. Phys. Lett.* **96**, 212501 (2010).
22. Taniguchi, T., Imamura, H., Nakatani, T. M. & Hono, K. Effect of the number of layers on determination of spin asymmetries in current-perpendicular-to-plane giant magnetoresistance. *Appl. Phys. Lett.* **98**, 4–6 (2011).
23. Li, S., Takahashi, Y. K., Furubayashi, T. & Hono, K. Enhancement of giant magnetoresistance by L21 ordering in Co2Fe(Ge0.5Ga0.5) Heusler alloy current-perpendicular-to-plane pseudo spin valves. *Appl. Phys. Lett.* **103**, 042405 (2013).
24. Chumak, O. M. et al. Magnetoelastic interactions and magnetic damping in Co2Fe0.4Mn0.6Si and Co2FeGa0.5Ge0.5 Heusler alloys thin films for spintronic applications. *Sci. Rep.* **11**, 76084 (2021).
25. Varaprasad, B. S. D. C. S. et al. Spin polarization and Gilbert damping of Co 2Fe(Ga xGe 1–x) Heusler alloys. *Acta Mater.* **60**, 6257–6265 (2012).
26. Kushwaha, V. K. et al. Prediction of half-metallic gap formation and Fermi level position in Co-based Heusler alloy epitaxial thin films through anisotropic magnetoresistance effect. *Phys. Rev. Mater.* **6**, 064411 (2022).
27. Takahashi, Y. K. et al. Large magnetoresistance in current-perpendicular-to-plane pseudospin valve using a Co2 Fe (Ge0.5 Ga0.5) Heusler alloy. *Appl. Phys. Lett.* **98**, 152501 (2011).
28. Li, S., Goripati, H. S., Takahashi, Y. K., Furubayashi, T. & Hono, K. Current-perpendicular-to-plane giant magnetoresistance in pseudo spin valves with Co2Fe(Ge0.5Ga0.5) heusler alloy ferromagnetic layers and Cu/Ag spacer. *IEEE Trans. Magn.* **49**, 4413–4416 (2013).
29. Du, Y., Varaprasad, B. S. D. C. S., Takahashi, Y. K., Furubayashi, T. & Hono, K. 001 textured polycrystalline current-perpendicular-to-plane pseudo spin-valves using Co2Fe(Ga0.5Ge0.5) Heusler alloy. *Appl. Phys. Lett.* **103**, 202401 (2013).
30. Goripati, H. S., Furubayashi, T., Takahashi, Y. K. & Hono, K. Current-perpendicular-to-plane giant magnetoresistance using Co 2Fe(Ga1-xGex) Heusler alloy. *J. Appl. Phys.* **113**, 043901 (2013).
31. Chen, J., Li, S., Furubayashi, T., Takahashi, Y. K. & Hono, K. Crystal orientation dependence of current-perpendicular-to-plane giant magnetoresistance of pseudo spin-valves with epitaxial Co2Fe(Ge 0.5Ga0.5) Heusler alloy layers. *J. Appl. Phys.* **115**, 233905 (2014).
32. Jung, J. W., Sakuraba, Y., Sasaki, T. T., Miura, Y. & Hono, K. Enhancement of magnetoresistance by inserting thin NiAl layers at the interfaces in Co2FeGa0.5Ge0.5/Ag/Co2FeGa0.5Ge0.5 current-perpendicular-to-plane pseudo spin valves. *Appl. Phys. Lett.* **108**, 102408 (2016).
33. Chikaso, Y. et al. Effect of off-stoichiometric composition on half-metallic character of Co2Fe(Ga,Ge) investigated using saturation magnetization and giant magnetoresistance effect. *J. Phys. D. Appl. Phys.* **55**, 345003 (2022).
34. Büker, B. et al. Elucidation of the strong effect of an interfacial monolayer on magnetoresistance in giant magnetoresistive devices with current perpendicular to the plane. *Phys. Rev. B* **103**, L140405 (2021).
35. Taparia, D. et al. Improvement in CPP-GMR read head sensor performance using [001]-oriented polycrystalline half-metallic Heusler alloy Co2FeGa0.5Ge0.5 and CoFe bilayer electrode. *Sci. Technol. Adv. Mater.* **25**, 2388503 (2024).
36. Hase, N., Nakatani, T. M., Kasai, S., Takahashi, Y. K. & Hono, K. Enhancement of current-perpendicular-to-plane giant magnetoresistance by insertion of Co50Fe50 layers at the Co 2Mn(Ga0.5Sn0.5)/Ag interface. *J. Appl. Phys.* **109**, 10–13 (2011).
37. Fujita, Y. et al. Spin-scattering asymmetry at half-metallic-ferromagnet|ferromagnet interface. *Phys. Rev. B* **104**, L140403 (2021).

38. Chen, Z. et al. Phase stability and half-metallic character of off-stoichiometric Co2FeGa0.5Ge0.5 Heusler alloys. *J. Appl. Phys.* **132**, 0–10 (2022).

39. Goto, K. et al. Effects of the atomic order on the half-metallic electronic structure in the C o2Fe(G a0.5 G e0.5) Heusler alloy thin film. *Phys. Rev. Mater.* **4**, 114406 (2020).

40. Husain, S. et al. Spin pumping in ion-beam sputtered C o2FeAl/Mo bilayers: Interfacial Gilbert damping. *Phys. Rev. B* **97**, 064420 (2018).

41. Suto, H., Nakatani, T., Asam, N., Iwasaki, H. & Sakuraba, Y. Evaluation of spin-transfer-torque efficiency using magnetization reversal against a magnetic field: comparison of FeCr with negative spin polarization and NiFe. *Appl. Phys. Express* **16**, 013003 (2023).

42. Barwal, V., Suto, H., Taniguchi, T. & Sakuraba, Y. Detailed and high-throughput measurement of composition dependence of magnetoresistance and spin–transfer torque using a composition-gradient film: application to Co x Fe 1−x (0 ≤ x ≤ 1) system. *Sci. Technol. Adv. Mater. Methods* **3**, 2286944 (2023).

43. Barwal, V. et al. Effect of stoichiometry and film thickness on the structural and magnetization dynamics behavior of Co2MnAl thin films cosputtered on Si(1 0 0). *J. Magn. Magn. Mater.* **552**, 169246 (2022).

44. Ghosh, A., Auffret, S., Ebels, U. & Bailey, W. E. Penetration depth of transverse spin current in ultrathin ferromagnets. *Phys. Rev. Lett.* **109**, 127202 (2012).

45. Behera, N., Singh, M. S., Chaudhary, S., Pandya, D. K. & Muduli, P. K. Effect of Ru thickness on spin pumping in Ru/Py bilayer. *J. Appl. Phys.* **117**, 17A714 (2015).

46. Suto, H. et al. Negative spin polarization of Mn2VGa Heusler alloy thin films studied in current-perpendicular-to-plane giant magnetoresistance devices. *J. Appl. Phys.* **135**, 203901 (2024).

47. Suto, H. et al. Negative spin polarization and effect of composition on the atomic order and electronic structure of Mn2VAl Heusler alloy thin films. *Phys. Rev. Mater.* **8**, 114408 (2024).

48. Sepehri-amin, h. et al. Journal of Magnetism and Magnetic Materials Design of spin-injection-layer in all-in-plane spin-torque-oscillator for microwave assisted magnetic recording. *J. Magn. Magn. Mater.* **476**, 361–370 (2019).

49. Barwal, V. et al. Large magnetoresistance and high spin-transfer torque efficiency of Co2Mn x Fe1−x Ge (0 ≤ x ≤ 1) Heusler alloy thin films obtained by high-throughput compositional optimization using combinatorially sputtered composition-gradient film. *APL Mater.* **12**, 111114 (2024).

50. Taniguchi, T., Yakata, S., Imamura, H. & Ando, Y. Penetration depth of transverse spin current in ferromagnetic metals. *IEEE Trans. Magn.* **44**, 2636–2639 (2008).

Acknowledgements

Author contributions

V.B. performed the experiments, conceptualized and conducted the formal analysis, and wrote the manuscript. H.S. and Y.S. contributed to conceptualization, analysis, validation, visualization, manuscript review and editing, and supervised the overall project.

Declarations

Competing interests

The authors declare no competing interests.

Additional information

Supplementary Information The online version contains supplementary material available at https://doi.org/10.1038/s41598-025-31714-7.

Correspondence and requests for materials should be addressed to H.S.

Reprints and permissions information is available at www.nature.com/reprints.

Publisher's note Springer Nature remains neutral with regard to jurisdictional claims in published maps and institutional affiliations.